Computers in Biology and Medicine 41 (2011) 960–970

Contents lists available at SciVerse ScienceDirect

Computers in Biology and Medicine

journal homepage: www.elsevier.com/locate/cbm

Automatic colposcopy video tissue classification using higher order entropy-based image registration

Juan D. García-Arteaga [a,*], Jan Kybic [a], Wenjing Li [b]

[a] Center for Machine Perception, Czech Technical University, Department of Cybernetics, Faculty of Electrical Engineering, Prague, Czech Republic
[b] STI Medical Systems, 4275 Executive Square #825, La Jolla, California 92037, USA

ARTICLE INFO

Article history:
Received 8 September 2010
Accepted 29 July 2011

Keywords:
Image registration
Colposcopy
Cervical cancer
Computer-aided diagnosis

ABSTRACT

Colposcopy is a well-established method to detect and diagnose intraepithelial lesions and uterine cervical cancer in early stages. During the exam color and texture changes are induced by the application of a contrast agent (*e.g.*3–5% acetic acid solution or iodine). Our aim is to densely quantify the change in the acetowhite decay level for a sequence of images captured during a colposcopy exam to help the physician in his diagnosis providing new tools that overcome subjectivity and improve reproducibility. As the change in acetowhite decay level must be calculated from the same tissue point in all images, we present an elastic image registration scheme able to compensate patient, camera and tissue movement robustly in cervical images. The image registration is based on a novel multi-feature entropy similarity criterion. Temporal features are then extracted using the color properties of the aligned image sequence and a dual compartment tissue model of the cervix. An example of the use of the temporal features for pixel-wise classification is presented and the results are compared against ground truth histopathological annotations.

1. Introduction

Uterine cervical cancer is the second most common form of cancer among women worldwide and the most common among women under 35 years. Unlike other more aggressive cancers, cervical cancer tends to be slow growing, with a development rate of several years. During the early pre-cancerous stages it may be completely asymptomatic with preinvasive cervix lesions only detectable by specific screening methods. When detected and treated early, cervical cancer has a recovery rate of nearly 100%. Nowadays, the main screening tool in cancer prevention programs is the Pap smear test, *i.e.* visual inspection of cells collected from the ectocervix. Although the use of the Pap test has led to a significant reduction in the cases of cervical cancer [1], it is not a diagnostic but a screening tool with high specificity and low sensitivity (94% and 72% respectively according to [2]).

Colposcopy is a well-established diagnostic method for early cervical cancer detection performed during a gynecological examination following an abnormal Pap smear test [3,4]. During the exam an expert (colposcopist) observes the cervix through a low magnification microscope (colposcope) in search of intraepithelial lesions following the topical application of a contrast-enhancing agent such as lugo-iodine, toluidine blue or, most commonly, acetic acid solutions. He then reports his findings and, if necessary, recommends a biopsy to confirm the diagnosis. The malignancy of the tissue is defined based on the form of the lesion's margin, the underlying vascular pattern and the degree of staining. When the applied contrast agent is low concentration acetic acid (3–5%) the abnormal acetowhite epithelium varies from a faint or bright white to a dense gray white color. It has been shown that the amount of whiteness is proportional to the severity of Cervical Intraepithelial Neoplasia (CIN). Furthermore, the opacity or translucency of the acetowhite reaction varies across the spectrum of CIN: normal metaplasia and low-grade lesions usually appear faintly white or slightly translucent whereas the acetowhite reaction of high-grade lesions appears more opaque. Acetowhite epithelium is, therefore, one of the major diagnostic features to detect cancer and pre-cancerous regions. Envisioned CAD systems aim to aid the physician in his diagnosis by quantitatively measuring and combining these diagnostic features with the analysis of high resolution images captured during the colposcopy exam [5]. This will result in more reliable diagnosis, minimization of the variability among colposcopists and the proportion of false positives leading to unnecessary biopsies. In this article we describe a system for automatic evaluation of colposcopic video sequences. Its key component is an image registration algorithm to compensate the spatial misalignment of individual frames.

* Corresponding author.
E-mail addresses: garcia@fel.cvut.cz (J.D. García-Arteaga), kybic@fel.cvut.cz (J. Kybic), wli@sti-hawaii.com (W. Li).

0010-4825/$ - see front matter © 2011 Elsevier Ltd. All rights reserved.
doi:10.1016/j.compbiomed.2011.07.010

1.1. Colposcopy temporal change measurement

Previous publications have proposed measuring temporal changes in color properties by comparing the information extracted from multiple images of the cervix and evaluating its color evolution through time, *i.e.* by extracting temporal features. In [6] the authors examined different regions of interest of images from a time sequence digitally captured during a standard colposcopy. Intensity normalization was done by using the ratio of the green/red color channels and patient movements were compensated by manual correction. The resulting intensity curve was linearly fitted for times before and after 200 s and the slopes of the lines, together with the average intensities of the first 0–100 s and between 200 and 300 s, were used to discriminate between normal tissue and CIN II (moderate dysplasia) to III (severe dysplasia or *carcinoma in situ*). In [7] a multi-spectral imaging colposcopic system was used to capture images during a colposcopy exam. Temporal curves of the intensity of backscattered light (IBSL) at 550 ± 25 nm with light polarization during the acetowhite decay process were analyzed to extract two temporal features (decay time and maximal aceto reaction). A clinical study of a similar procedure using a wavelength of 525 ± 25 nm was presented in [8]. The extracted features were correlated to six cervical conditions of the underlying tissue: CIN I (mild dysplasia), II, III, normal mature epithelium, immature metaplasia and inflammation.

1.2. Cervical image movement compensation

In the reviewed literature movement compensation, when present, is limited to manual correction. However, manual correction is known to be time consuming, subjective and mostly inaccurate [9]. In [8] the manual image correction procedure compensated only for translations as, reportedly, "the measurement geometry did not allow any rotation of the cervix". Yet, geometric compensation is vital for any kind of temporal analysis as the data can be corrupted or, in some cases, rendered useless by the movement of the object being analyzed. Restricting the patient's movement may reduce the problem but is cumbersome and uncomfortable; furthermore it does not prevent other movement sources such as camera movement, breathing, involuntary muscle contractions or elastic tissue deformation. A better alternative is to adapt one of the many retrospective image registration algorithms from computer vision [10,11] and medical imaging [12–14].

Some image-registration schemes based on the iterative minimization of a simple similarity criterion have been already used for cervical images. Most of the methods proposed use simple similarity criteria (such as the sum of square differences [15,16] or correlation [17–19]) which will only work properly for images taken at short time intervals (when the appearance changes are small). As the time lapse between captures increases these systems tend to fail due to progressive appearance changes of the cervix induced by the acetic acid, changes in the illumination direction and the appearance of new objects in the field of view (e.g. glints, mucous, blood spots). An alternative to similarity criteria minimization was presented in [20] where consecutive frames of a colposcopy video sequence were affinely registered via feature-based registration. The transformations were then composed to obtain the transformations between non-consecutive frames. The basic assumption was that the region of interest (ROI) in the cervix could be treated as a planar surface and registered to any other image by a homography. It should be noted that, with the exception of [15,16] which use elastic transformations and sum of square differences criterion (SSD), all proposed methods use rigid 2D transformation (in many cases simple translations) which cannot compensate the movement of the scene due to the change of camera viewpoint motion nor the elasticity of the tissue being imaged.

1.3. Previous work

It has been shown that the use of multiple features may improve the registration results in difficult or noisy images [21–23]. We proposed, in a previous publication [24], the use of a multi-feature similarity criterion for the registration of colposcopy images as an alternative to gray-scale Mutual Information (MI) calculated via joint histograms. The evaluation protocol proposed by [25] was used to asses the capture range, accuracy and risk of non-convergence of multi-feature similarity criteria vs. histogram-based MI on image pairs with known ground truth, *i.e.* "gold standard" registrations. For these tests, the joint entropy criterion using multiple neighbors gave consistently the best results. Further tests with colposcopy image sequences showed an improvement of robustness and accuracy when using the multi-feature entropy criterion instead of histogram-based MI.

Due to the high number of dimensions involved the entropy was calculated using the Kozachenko–Leonenko (KL) estimator [26,27] instead of joint histograms. The KL estimator calculates the entropy of a distribution using N_S samples and the l_2 distance between each sample $\mathbf{l}(n) \in \mathbb{R}^D$ and its nearest neighbor $\mathbf{l}_{NN}(n)$ among the N_S-1 remaining samples

$$\mathcal{H}_{KL}^{N_S}(\mathbf{l}) = \frac{D}{N_S}\sum_{n=1}^{N_S} \log(\|\mathbf{l}(n)-\mathbf{l}_{NN}(n)\|)+K \tag{1}$$

$$K = \log\frac{(N_S-1)\pi^{D/2}}{\Gamma\left(1+\frac{D}{2}\right)}+\gamma \tag{2}$$

where γ is the Euler constant and D is the number of dimensions.

For discrete valued images the probability of a "crash" (two samples having the same value) is not zero, we therefore use a modified robust entropy estimator [28,29]

$$\mathcal{H}_{DKL}^{N_S}(\mathbf{l}) = \frac{D}{N_S}\sum_{n=1}^{N_S} \log(\max(\|\mathbf{l}(n)-\mathbf{l}_{NN}(n)\|,\varepsilon)+K \tag{3}$$

Here ε is the minimum distance between element pairs used in the entropy calculation. This corresponds to taking into account quantization and bounds the absolute value of $\mathcal{H}_{DKL}$.

1.4. Proposed method

In the present article we propose a full elastic cervical image registration scheme which uses a novel multi-modal similarity criterion based on the high-order image entropy estimation described in the previous section [26,27] to register the cervical image sequences and solve the spatial distortions. We have derived a new measure of acetowhiteness based on the registered aceto-sequence/pre-aceto image pair difference of color saturation S in the Hue-Saturation-Intensity color space (*HSI*) [30]. This measure is robust to the variations induced from illumination changes and avoids the additional uncertainty added when using shading correction techniques [31] or retrospective illumination correction methods [20].

Finally we fitted the discrete samples of the acetowhiteness to a biologically plausible mathematical model derived from multi-compartment analysis of the decay process and used the resulting features for classification.

The article is organized as follows: Section 2 describes the components of the proposed image registration algorithm (2.1) and the extraction of the temporal acetowhite curve (2.2). Section 3 describes the datasets and methods used for the image registration

and temporal feature validation and the results. Conclusions are presented Section 4.

2. Method

2.1. Image registration

2.1.1. Region of interest selection

Illumination changes can strongly modify the visible portion of the cervix in different images. If an ROI mask is not used, pixel-based optimization algorithms tend to align the two backgrounds (in this case the shaded areas and the opaque speculum used to separate vaginal walls, as seen on Fig. 1) and not the cervix's visible features. To avoid this an ROI approximately separating the cervix from the background is automatically detected in the fixed image [32]. Registration is done between the masked template image and all the other (non-masked) images of the sequence.

2.1.2. Initialization

The initial geometrical displacement differences between the images due to camera and patient movement can be quite large, in some cases over 100 pixels (see Fig. 2). The registration algorithm needs to be initialized within the convergence basin of the true solution. To do this, a small rectangular template was automatically cropped from the fixed image's ROI's central area and matched by maximization of normalized cross-correlation (NCC) to all other sequence images. The initial translation is equal to the displacement vector between the template's center position and the NCC's maximum. The NCC calculation can be done extremely fast by calculating cross-correlation in the frequency domain and pre-computing integrals of the image over the search window [33]. The size of the window depends on the image size and is chosen to roughly cover the external orifice of the uterus (or external os) which is an area rich in visual detail.

2.1.3. Similarity criterion

Choosing an appropriate similarity criterion is possibly the most delicate part of the image registration algorithm design. We have chosen a similarity criterion adapted to multi-modal image registration due to the varying reactions of the different tissue types after the application of the contrast agent, as seen on Fig. 1.

The proposed similarity criterion for registering images f and g is the entropy of vectors $\mathbf{f^2}$ and $\mathbf{g^2}$, consisting of the pixel at position $\mathbf{x}_{ij}$ and two of its immediate neighbors

$$\mathbf{f^2}(\mathbf{x}_{ij}) = [f(i,j), f(i+1,j), f(i,j+1)] \tag{4}$$

The entropy is calculated using the estimator $\mathcal{H}_{DKL}$ explained in Section 1.3. Two neighbors were chosen instead of a larger vicinity as a trade-off between accuracy and speed. Results in [24] show that the loss in accuracy is relatively small whereas the speed improvement is substantial.

2.1.4. Transformation

Image registration is done in three consecutive steps. The first step, initialization, was described in Section 2.1.2. The second step consists of a rigid registration that compensates most of the gross movement errors and makes areas with equivalent tissue overlap. The results of this step are used as the starting point for an elastic image registration algorithm using the same similarity criterion.

The rigid registration consists of a 2D translation and a rotation. We define this transformation as

$$\mathbf{g}_{(\theta,\mathbf{T},\mathbf{C})}(x',y') = \mathbf{g}(x,y) \tag{5}$$

where θ is the rotation angle, (C_x,C_y) are the coordinates of the rotation center and (T_x,T_y) are the components of the translation. The rotation center C is chosen to coincide roughly with the center of the Os region, a dark circular or elongated zone at the center of the cervix which corresponds to the end of the uterine cavity.

We use a multiresolution B-spline pyramid to represent the elastic deformation [35]. This deformation model has been

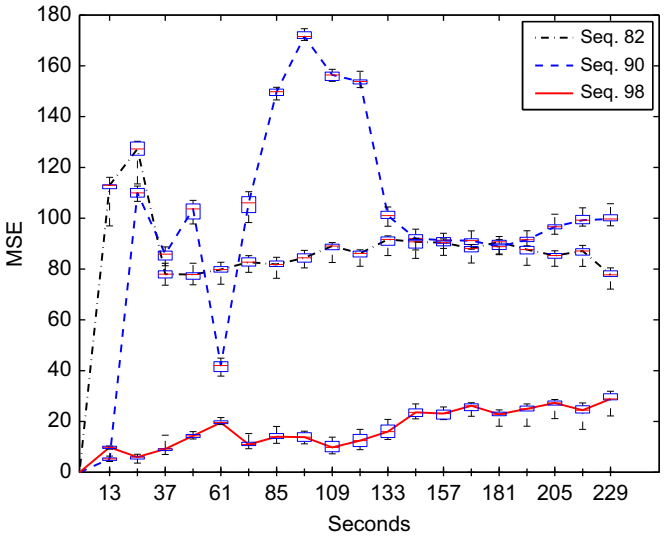

Fig. 2. Mean initial geometrical error (before the registration) in pixels. Error is calculated as the mean distance between the transformed landmarks of each image and those of the first image of the sequence [34].

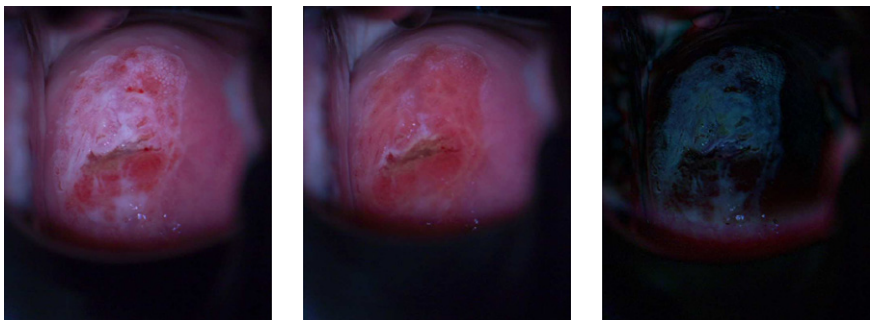

Fig. 1. In images taken near the point of maximum acetowhitening the metaplastic epithelium turns opaque white (left). As time passes this tissue changes back to its original color whereas normal epithelium remains mostly unchanged (center). The inhomogeneity of the color changes may be seen in the image difference of two images (right). The difference between images taken at short intervals (*e.g.* less than a few seconds), is almost imperceivable except for glint.

studied and used extensively in medical imaging. In our case the deformation is parametrized by a finite number of parameters $\mathbf{c_l}$:

$$\mathbf{g_c} = \mathbf{x} + \sum_{\mathbf{l} \in I_c \subset \mathbb{Z}^N} \mathbf{c_l} \beta_q(\mathbf{x}/\mathbf{h} - \mathbf{j}) \tag{6}$$

where β_q is the tensor product of B-splines of degree q and $\mathbf{h}$ is the knot spacing. In 2D, this is equivalent to constructing a regular grid of knots and associated coefficients over the moving image. As rigid transformations can be exactly described by B-Splines, the results of the rigid registration can be used as a starting point without any loss of precision and with minimal overhead.

2.1.5. Optimization

The rigid registration is defined as the minimization of the similarity criterion $\mathcal{H}_{DKL}$ over rigid transformation parameters for all (i,j) contained within the ROI:

$$\arg \min_{\theta, T_x, T_y} \mathcal{H}_{DKL}(\mathbf{f}^2(i,j), \mathbf{g}^2_{(\theta,\mathbf{T},\mathbf{C})}(i,j)) \tag{7}$$

To find the minimizer of this equation we use the robust NEWUOA algorithm [36], an extension of Powell's UOBYQUA algorithm for unconstrained optimization without derivatives [37]. Additionally, we use multi-scale registration to avoid local minima and reduce computation time.

The elastic optimization problem is defined by replacing the deformation generator in Eq. (7):

$$arg \min_{\mathbf{c_l}} \mathcal{H}_{DKL}(\mathbf{f}^2(i,j), \mathbf{g}^2_{(\mathbf{c_l})}(i,j)) \tag{8}$$

We have used the Fletcher–Reeves conjugate gradient algorithm [38] in the elastic registration step instead of NEWUOA. The former algorithm approaches the minimum by a series of line minimizations in a sequence of search directions p calculated using the minimized function's gradient. While the NEWUOA algorithm is fast and robust, it is limited to search spaces with a relatively low number of dimensions. To calculate the gradient of the similarity criterion $\mathcal{H}^{N_S}_{DKL}$ we have derived an analytic expression presented in Appendix A.

2.1.6. Evaluation speed

Each iteration of the optimization requires the deformation warping of the moving image and the reevaluation of the similarity criterion $\mathcal{H}^{N_S}_{DKL}$. Of these two operations, which must be performed repeatedly, the latter is by far the most time consuming due to the need of finding the nearest neighbor for each of the N_S elements of the ROI. A simple brute force approach has a complexity of $O(DN_S^2)$. In the present implementation we have used a best-bin first (BBF) bottom-up *kD* tree traversal search to find the approximate *NN*. To do this a *kD* tree with each leaf containing at most L samples is built at each iteration. The complexity of the search for all *NN*s is of $O(DN_S M)$, where M is a predetermined number of leaf-points to be visited defining the compromise between accuracy and speed. The total complexity of building the tree is $O(DN_S \log(N_S/L))$.

The present implementation of the registration running on an Intel Core i7 CPU at 2.67 GHz takes approximately 10 min to register the cervix area of two 750×1125 images.

2.2. Temporal feature extraction

Once the images of the cervical sequence are aligned we calculate the acetowhite decay rate for each pixel location. A curve of the quantitative "whiteness" measure against time is fitted to the acquired values to increase robustness and to summarize the information from the curve into a small number of parameters, which is useful for diagnostics/classification.

2.2.1. Whiteness measurement

We assume that the colposcopy images may be modeled by an image formation process based on a multiplicative interaction between the illumination $L(x,y)$ and the object $M(x,y)$ to produce an image $I(x,y)$:

$$I(x,y) = M(x,y)L(x,y) \tag{9}$$

We assume that M is related to the acetowhite level of the tissue at each pixel. If L was constant and known, it would be possible to calculate M from Eq. (9). However, due to the object's shape and movements, L is unknown.

As a workaround, we use a saturation S from the hue-saturation-intensity color space or HSI. The HSI is a cylindrical-coordinate representation of the RGB color-mode which is closer to the human perception of color. In particular, saturation S represents the relative intensity of the color, with 0 representing complete lack of color (*i.e.* pure gray-scale) and 1 full saturation. Keeping this in mind, we should expect the S value for a tissue location to be minimal at the point of maximal acetowhiteness and maximal at pre-aceto and post-aceto. We assume that the illumination does not change S. We define a measure A of acetowhiteness as

$$A(x,y,t) = 1 - (S(x,y,t) - S_{preaceto}(x,y)) \tag{10}$$

Here $S_{preaceto}(x,y)$ is the saturation value at (x,y) before the application of the acetic acid. Under normal circumstances the tissue will be more color saturated at this moment than after the application of the acid. The resulting values in Eq. (10) fall generally between 0 and 1 with minimum values at $t = 0$ s and the maximum at the point of minimal S. Note however that due to the sudden appearance and disappearance of blood spots (high color saturation) or glint (white and therefore completely void of color saturation) $A(x,y,t)$ may have values outside the [0,1] range.

2.2.2. Curve fitting

To extract features with diagnostic value and filter noise from the available data we have fitted a continuous function to the acetodecay samples using a mathematical model of the tissue's interaction with the acetic acid. Different models have been used previously: two straight lines [6], an ellipse (for the ascending part) [17], as well as a double [7] and triple exponential function [8]. An alternative for these *ad hoc* models are multi-compartment models [39]. Each compartment is assumed to be a homogeneous entity within which the entities being modeled are equivalent. In particular, the compartmental model has been useful in analyzing the metabolism and absorption rate of a substance in the human body. In [40], the authors showed how the epithelial tissue could be effectively modeled by a multi-level compartment model of the cervix. Each level represented a dysplastic layer and consisted of two compartments: one for extracellular and one for endocellular space. The number of levels of the model depends on the number of dysplastic layers and is known *a priori*. The system needs to set 20 model parameters related to physical quantities such as endocellular and exocellular pH levels, extracellular and intracellular volume, cell area, intracellular buffering, etc ... This is done using previously published values. For a complete list of the parameters and the used values please refer to [40].

We have chosen a much simpler and intuitive dual compartment open model shown in Fig. 3. As in [40], we interpret compartment 1 as the extracellular space and q_1 as the concentration of topically applied acetic acid which has not yet been absorbed by the epithelia. Compartment 2 is then the intracellular space and q_2 the concentration of absorbed applied acetic acid before it is assimilated and carried away by the blood-stream. We assume q_2 to be proportional to A.

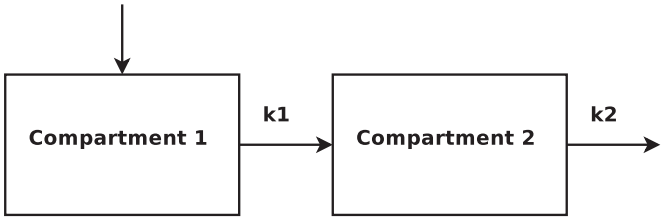

Fig. 3. Graphical representation of the two compartment open catenary model used.

In this model, the tracer/transmitted substance is initially contained in compartment 1 and flows to compartment 2 at a rate of k_1. The tracer leaves the system from compartment 2 at a rate of k_2. The quantities q_1 in compartment 1 and q_2 in compartment 2 are modeled by

$$\frac{dq_1}{dt} = -k_1 \cdot q_1 \tag{11}$$

$$\frac{dq_2}{dt} = k_1 \cdot q_1 - k_2 \cdot q_2 \tag{12}$$

The solutions of these equations are a sum of exponential functions:

$$q_1 = C \cdot e^{-k_1 t} \tag{13}$$

$$q_2 = C \frac{k_1}{k_1 - k_2}(e^{-k_2 t} - e^{-k_1 t}) \tag{14}$$

We use Eq. (14) (the quantity in the second compartment) to fit sequence A in time in the least squares sense at each image position (x,y), *i.e.* we search numerically for k_1 and k_2 that minimize

$$F = \sum_{\forall n}(q_2(t_n) - A(x,y,t_n))^2 \tag{15}$$

Note that the constant term C arises. This term corresponds to the concentration level of q_1 at $t=0$ and is not related to the tissue's physical properties. Since we have no independent measure of q_1 nor any initial condition constraint it is not possible to find its exact value. We have therefore assumed C to be equal to 1 (maximum possible concentration) for all image locations.

3. Results

3.1. Image acquisition

Two different image datasets were used to test the accuracy of the image registration algorithm proposed.

3.1.1. Dataset 1 (STI)

Women 22–50 years old with previously detected abnormal cervical cytologic abnormalities, a concordant colposcopic diagnosis and scheduled for an electrosurgical loop excision procedure were asked to enroll in the trials conducted at Hospitals in Lima and Cusco, Peru. All subjects read and signed an institutional review board approved informed consent document. Exclusion criteria included cervical hemorrhage, pregnancy, and unwillingness to participate.

During the exam, a 5% acetic acid solution was applied with solution-soaked cotton balls placed in contact with the surface of the cervix for 1 min. High resolution 750×1125 16-bit RGB images were captured with and without a cross-polarized filter to reduce glint and a black opaque speculum was used to cancel the background and separate the vaginal walls.

The cervical sequences were composed of 33 images taken at intervals of 5 and 12 s before and after the moment of maximal acetowhiteness, respectively. The first image was captured immediately after removing the cotton ball and the final image was captured approximately 300 s later. Additionally, a preaceto image was captured immediately before the application of the acetic acid.

3.1.2. Dataset 2

The second dataset is publicly available[1] and consists of 10 colposcopic image sequences of women between 22 and 35 years old with abnormal Pap smear tests, all of whom gave informed written consent [19].

The colposcopy was done using 3 ml of acetic acid (3%) spread over the cervix using a needle. Color images of 352×240 pixels were acquired every second during the 10 s before and the 5 min after acetic acid application. Each image was saved independently as a BMP file. Full acquisition details may be found in [41].

3.2. Aceto-PostAceto registration validation

Presently, there is no *gold standard* against which to measure the registration's accuracy for cervical images. External markers such as small paper dots attached to the cervix or marks made with a surgical pen have been used for referencing purposes [42] but their use as fiducial markers is limited as the paper dots may move and the ink diffuses.

Instead, to measure the registration error, we have automatically generated and matched salient features from the colposcopic image sequences following the procedure described in [34]. The features' locations show the position of the same tissue in different images of the sequences and can therefore be used as landmarks. These landmarks were manually checked to confirm that they corresponded to the same location and mismatches were rejected. Dataset 1 consisted of four sequences of twenty images taken every 12 s and Dataset 2 of ten sequences of twenty images taken every 10 s. Image acquisition for both datasets begins 120 s after acetic acid application. All images were registered to the first image of the series and error was calculated as the average euclidean distance between the position of each of the M landmarks at t_0, $(x^m_{t_0}, y^m_{t_0})$, and the final position of their corresponding landmarks at times $[t_1, t_2, \ldots, t_N]$ after registration, $(x^m_{t_n}, y^m_{t_n})'$:

$$Err = \frac{1}{M} \cdot \frac{1}{N} \sum_{n=1}^{N} \sum_{m=1}^{M} \sqrt{(x^m_{t_0} - (x^m_{t_n})')^2 + (y^m_{t_0} - (y^m_{t_n})')^2} \tag{16}$$

Results can be seen in Fig. 4 and are summarized in Table 1.

For comparison, we have repeated the registration process with previously presented and validated registration algorithms to compare their performance with these images against our proposed method (HDKL). The alternate registration methods used are the Image Registration ToolKit (IRTK) and the Generalized Dual-Bootstrap ICP algorithm (GDB); the former is a point-based iterative scheme that uses gradient-based optimization of a similarity criteria, in this case normalized mutual information (NMI) [43–45] and the later is a robust state-of-the-art algorithm driven by the matching of multi-scale features [46]. To ensure a fair comparison, IRTK registration used the initialization described in Section 2.1.2, a masked reference image, and a rigid + elastic registration scheme. The fixed image ROI mask was used for GDB. Executable programs of both algorithms are available from the respective authors' web pages.[2,3]

[1] http://www.uv.mx/heacosta/.
[2] http://www.doc.ic.ac.uk/~ dr/software/.
[3] http://www.vision.cs.rpi.edu/gdbicp/exec/.

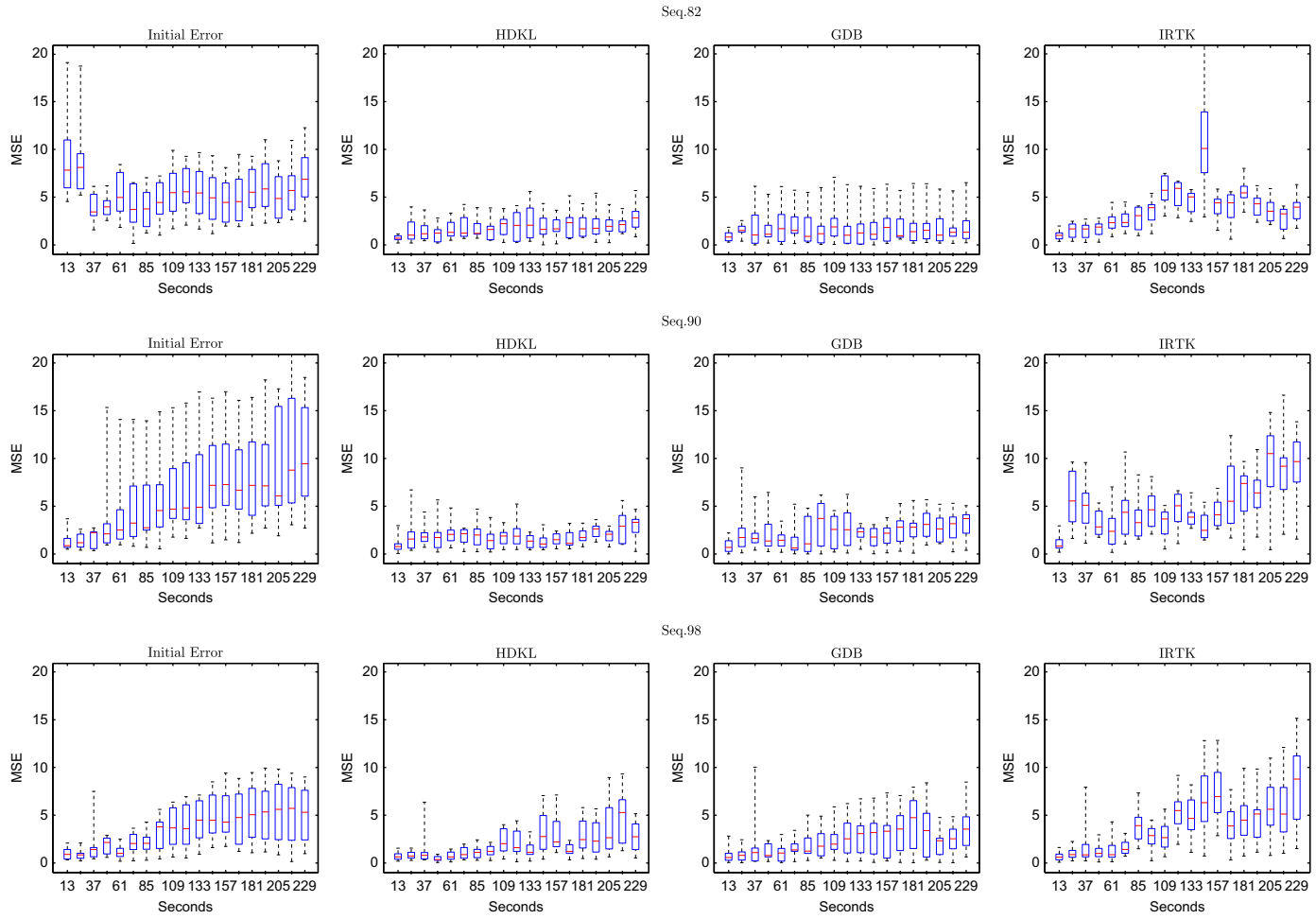

Fig. 4. Boxplots of the error distribution of the landmarks after registering all images of the sequence to the reference acetowhite image. Each column corresponds to a different registration method and the *x*-axis shows the capture time difference between the two images in seconds.

In Table 1 it can be seen how the initial error calculated from the original landmark positions ("Unregistered" column) is significantly reduced when using the fast NCC template matching technique explained in Section 2.1.2 ("Initialized" column). In some of the presented cases this error reduction was of one order of magnitude. The fact that this method requires only the approximate location of one point within the fixed image ROI makes it less error prone than methods requiring the automatic extraction of equivalent points in all other sequence images (*e.g.* by finding the centroid of automatically extracted ROIs) and less labor intensive than manual initialization.

HDKL and GDB proved to be the most accurate and robust of the tested methods. The GDB performed slightly better on Dataset 2 (all median and mean GDB errors and all but one of HDKL's are under 1 pixel) and HDKL performed slightly better on Dataset 1 (all median and mean HDKL errors and around half of GDB's are under 2 pixels). These small mean and median errors indicate an overall good and reliable registration for both methods.

The IRTK elastic registration algorithm using NMI reduces consistently average errors with respect to the initialization, although not as much as the elastic HDKL. It also presents some high maximum errors and misregistration (*e.g.* Seq. 82 with a maximum error of over 30). This error was due mostly to elastic over-fitting even though a penalty $\lambda = 10^{-5}$ term was added to the similarity metric during registration using IRTK to preserve smoothness. Running the default settings for IRTK, *i.e.* smoothness regularization $\lambda = 0$, results in major over-fitting artifacts. On the other hand, landmark errors and visual inspection confirm that the resulting elastic deformations calculated with HDKL and no regularization are correct.

It should be noted that in Dataset 1 the values of the registration vs. the initialized errors are reduced approximately by one half. In Dataset 2 the registration vs. initialized errors are also reduced although not so drastically as in Dataset 1. Furthermore, in some cases of Dataset 2 mere rigid initialization results in sub-pixel errors. Even taking into account the considerable difference in image sizes (Dataset 1 images are approximately three times larger than images in Dataset 2) these results indicate that for Dataset 1 there are stronger 3D movement and elastic displacement elements present that cannot be compensated by a 2D affine transformation.

3.3. Curve fitting and feature extraction

The original pre-aceto and acetowhite color images were converted to the *HSI* space. The *S* channel was extracted and geometrically transformed using the results of the registration step. Using Eq. (10), the acetowhiteness was calculated for each location within the ROI. The temporal samples were fitted to the curves at each pixel location within the ROI by solving Eq. (15) using the Levenberg–Marquardt algorithm. The fitted curves at three locations corresponding to low-grade squamous intra-epithelial lesion (LSIL), high-grade squamous intra-epithelial (HSIL) and normal epithelium may be seen in Fig. 5.

Table 1
Error measurements (given in pixels) for different registration methods and datasets. Best results per set in bold type. The "Unregistered" column corresponds to the error from the initial unregistered images and "Initialized" to the rigid alignment done using NCC.

	Unregistered	Initialized	HDKL	GDB	IRTK
Dataset 1					
Seq. 82					
Mean	88.34.	5.50	1.88	**1.84**	3.80
Median	86.47	5.27	1.57	**1.30**	3.28
Max.	130.30	19.08	**5.69**	7.07	31.82
Seq. 90					
Mean	101.84	4.77	**1.88**	2.27	5.06
Median	98.15	4.83	**1.74**	2.11	4.56
Max.	174.59	9.88	**6.71**	9.01	16.62
Seq. 98					
Mean	17.65	3.52	**1.95**	2.27	3.96
Median	16.89	2.62	**1.32**	1.70	3.27
Max.	31.90	9.88	**9.93**	10.03	15.14
Dataset 2					
Seq. 01					
Mean	8.60	0.82	0.43	**0.33**	0.44
Median	8.33	0.77	0.32	**0.29**	0.37
Max.	22.35	1.77	1.76	**0.97**	1.51
Seq. 02					
Mean	16.66	3.60	0.92	**0.89**	1.81
Median	15.31	1.49	**0.71**	0.79	1.42
Max.	36.50	25.23	3.58	**3.17**	11.81
Seq. 03					
Mean	20.098	1.24	0.99	**0.52**	2.26
Median	22.22	1.26	0.88	**0.43**	1.70
Max.	35.97	2.89	3.42	**1.32**	8.30
Seq. 04					
Mean	16.2	1.12	0.50	**0.48**	0.51
Median	12.33	0.73	0.43	**0.40**	0.41
Max.	41.82	3.52	1.51	**1.08**	1.55
Seq. 05					
Mean	7.98	1.05	0.52	**0.33**	0.73
Median	7.96	0.83	0.37	**0.25**	0.51
Max.	13.67	3.67	2.03	**1.19**	2.56
Seq. 06					
Mean	8.76	1.14	0.97	**0.41**	0.71
Median	7.50	0.98	0.75	**0.39**	0.68
Max.	23.71	2.69	4.48	**1.27**	1.82
Seq. 07					
Mean	20.60	2.14	1.06	**0.65**	1.31
Median	21.69	2.11	0.93	**0.53**	1.06
Max.	44.67	5.62	2.69	**2.21**	4.13
Seq. 08					
Mean	18.14	1.00	1.18	**0.62**	1.26
Median	18.41	0.86	1.17	**0.53**	1.03
Max.	34.47	3.45	2.78	**1.71**	3.61
Seq. 09					
Mean	10.50	1.03	0.67	**0.41**	1.09
Median	11.32	0.71	0.47	**0.41**	0.78
Max.	17.61	3.79	3.17	**0.97**	5.15
Seq. 10					
Mean	8.67	0.79	0.67	**0.35**	0.63
Median	8.69	0.69	0.52	**0.23**	0.54
Max.	17.47	2.81	3.30	**0.97**	2.35

From the fitted parameters four features were extracted for each non-masked pixel location: k_1, k_2, k_1/k_2, and maximal acetowhite reaction *maxw*. Two additional parameters m and b extracted from fitting the acetowhite samples $(t > 60)$ s to a straight line in a similar way as in [6] and corresponding to the slope and y-intercept were also used. The template image and *maxw* maps for different sequences may be seen in Fig. 6.

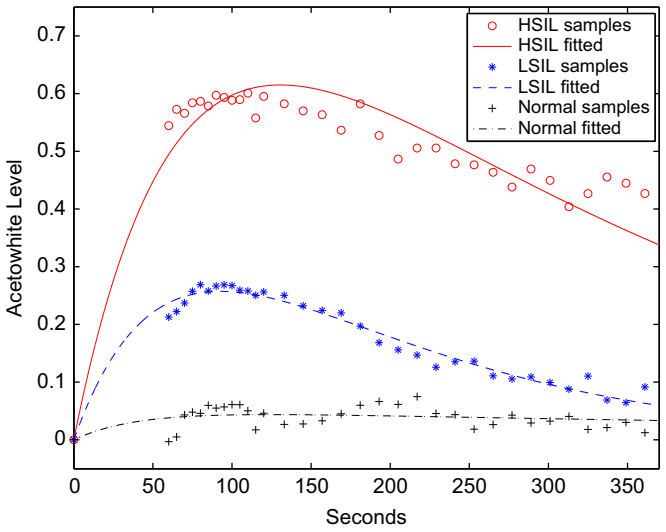

Fig. 5. Example of fitting the image samples from an image sequence (Seq. 06) to the compartment mathematical model. The y-axis corresponds to the calculated whiteness level (1 being the maximum whiteness value) and the x-axis corresponds to seconds after the application of acetic acid. The whiteness level of normal epithelium samples A_n does not change much in contrast to HSIL and LSIL samples in which a sharp change in the whiteness level occurs around 60 s.

3.4. Classification

The ultimate goal of registering the sequence and extracting temporal features is to be able to correctly classify the tissue as healthy or lesion and, if possible, to be able to classify the lesion's degree. A pixel-wise ground truth is needed both to train the classifier and to validate the results. We have used a novel pathology annotation extraction procedure to map detailed pathology annotations onto the digital image of the cervix. The full process is explained in detail in [47] but it can be briefly summarized in the following steps:

- A colposcopic image is acquired after applying acetic acid, referred as reference image.
- A loop electrosurgical excision procedure (LEEP) cone is acquired as necessary. The specimen is put in formalin and shipped to a pathology laboratory. The specimen is cut into serial blocks, a process known as "bread-loafing", from which one section is cut and put on a microscope slide.
- The slides are digitized using a slide scanner.
- The digital images are annotated using several different defined annotation layers.
- Using all gathered data regarding the tissue specimen, a semi-manual software is used to map the annotations back to the image of the cervix before the LEEP was acquired.
- A pathology map is created that is registered spatially to the reference image.

It should be noted that mapping the histopathologic slide annotation back to colposcopic image is a complex task due to deformations during excision and sectioning, and tissue shrinkage during formalin fixation. Since the tissue processing procedure involves works done at both the clinic site and histopathology lab, it is both a time-consuming and costly procedure. Examples of annotated pathology maps back mapped to the reference images are shown in Fig. 7.

The values for the temporal features described in Section 3.3 were extracted for image locations classified as normal epithelium, LSIL or HSIL in the image sequences 82 and 06. This gives

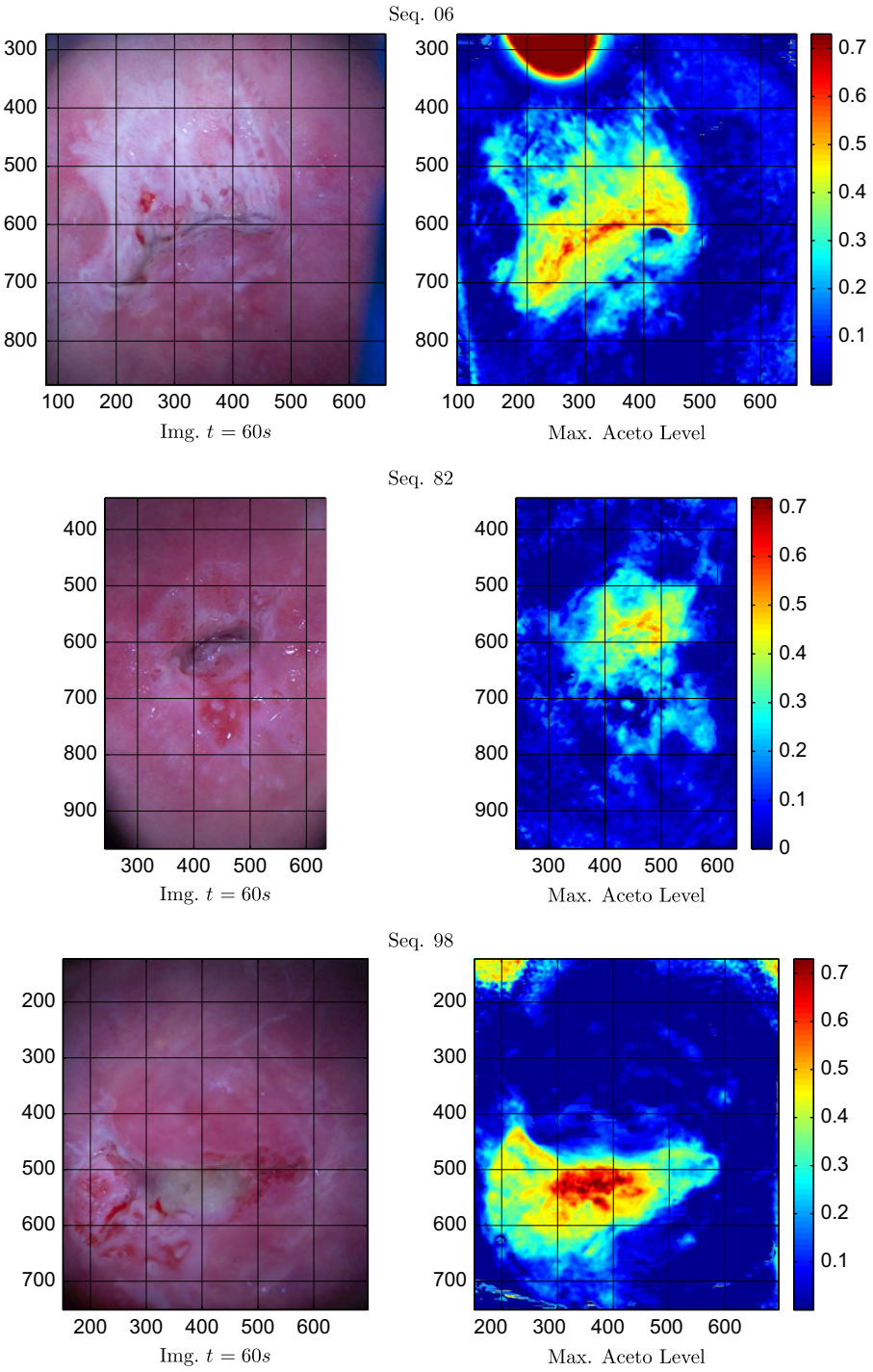

Fig. 6. Examples of the template image and the corresponding calculated maximal acetowhite reaction value. In Seq. 06, the blob with higher aceto level is caused by the unexpected shifting of the speculum to the cervix. In Seq. 98: the *maxw* peaks are introduced by mucus. This mucus may be physically removed during the clinic exam or be retrospectively compensated with other algorithms.

a total of 9335 pixel locations from both images. Of these 330 were discarded because the compartment model fitting diverged, leaving a total of 9005 valid points. A Support Vector Machine classifier (SVM) [48,49] using a radial basis kernel function was trained to label samples either as Normal or Abnormal. A second classifier was trained to classify an abnormal sample as either LSIL or HSIL.

For the abnormal vs. normal classifier a 5-fold cross validation was run with the full data set resulting in an average accuracy of 79.3% and an area under the curve (AUC) of 84.9%. The same procedure was repeated for the LSIL vs. HSIL classifier resulting in an average accuracy of 92.3% and an AUC of 87.3%. The ROC curve for both classifiers is shown in Fig. 8.

Although our test data is quite limited, the final results of the classification show that the extracted temporal features strongly correlate with the ground-truth. This is the first work, to the best of our knowledge, that relates histopathology findings with pixel-wise colposcopy image locations.

The results show that a pixel-wise classification is possible based only on features extracted from the acetowhitening decay curve. The classifier and training process need no further adaptation to add additional features, such as texture, or multi-spectral

imaging. From these individual pixel classifications it is possible to make an aggregate diagnostics for the whole sequence.

4. Conclusions

In the present article we have shown that it is possible to consistently register cervical sequences with elastic transformations. Furthermore, in the tests performed the proposed algorithm using a multi-feature similarity criterion outperformed IRTK, a well-known and tested algorithm using histogram-based MI. The small resulting error and the classification results from registered data indicate that the use of multiple features provides enough local information to correctly align the images.

Registration results showed a similar performance for HDKL (the proposed method) and GDB. It should be remembered that the landmarks used for comparison have an unknown localization error, probably of over 1 pixel. As in most sequences the mean and median error differences between HDKL and GDB are below a pixel (in some cases below a tenth of a pixel) their performances should be considered equivalent. It is not clear, however, if the GDB method will be able to cope with colposcopy images that present stronger elastic deformations and appearance changes (*e.g.* pre-aceto/aceto image pairs). Additionally, the fact that GDB registration software contains "copyrighted implementations of patented and patent-pending algorithms" and limits its use in future diagnostic systems.

In previous works only rigid transformations and derivative-free optimization had been used basically due to the time and computational power needed to calculate numerical gradients. In the present article, the use of complex elastic deformations and alternative optimization algorithms are made possible by the analytical expression of the spatial gradient of the $\mathcal{H}_{DKL}$ criterion. Extensions of these results to registration using more features, 3D volumes or MI based on DKL remain possible future research directions.

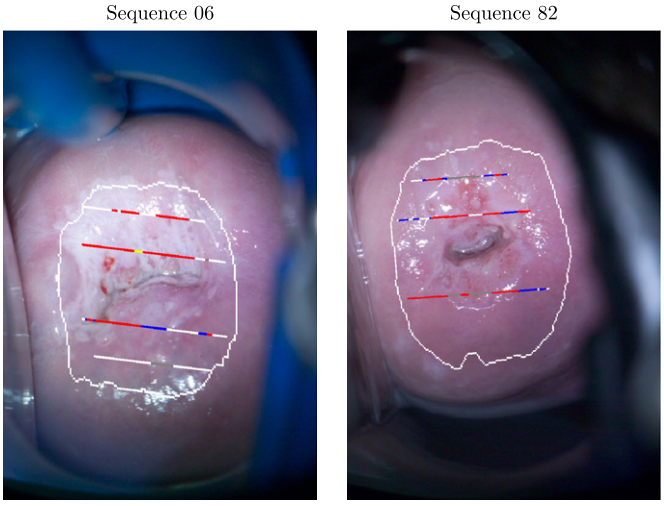

Fig. 7. Pathology maps overlayed on the reference image. The white contour corresponds to the LEEP outline. The straight lines color codes are: red line HSIL , blue line LSIL, yellow line microinvasion, white line normal epithelium and gray line burned epithelium or no information. (For interpretation of the references to color in this figure legend, the reader is referred to the web version of this article.)

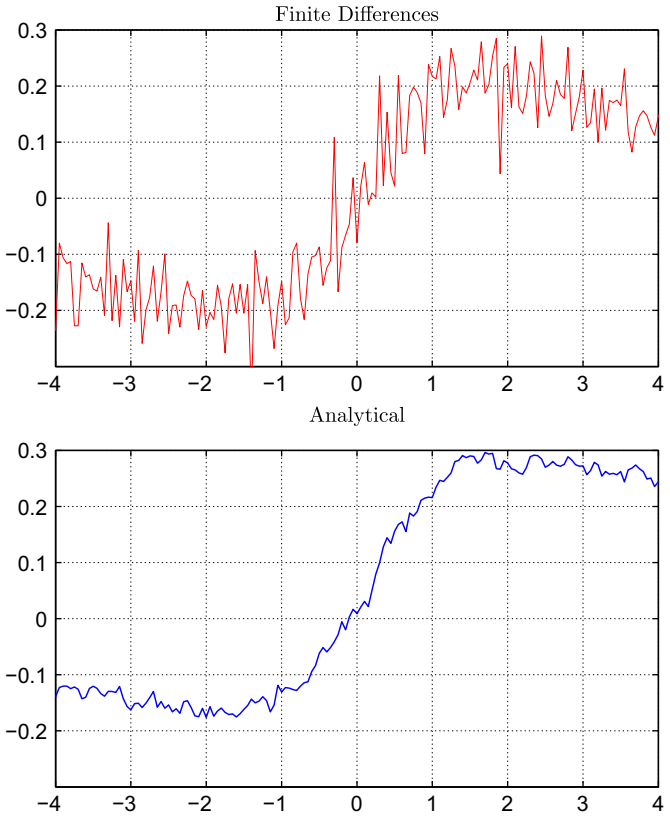

Fig. A.1. Comparison of the gradient of H_{DKL} along the displacement direction calculated using small displacements (0.05 pixels) and using the analytical expression derived from (A.3).

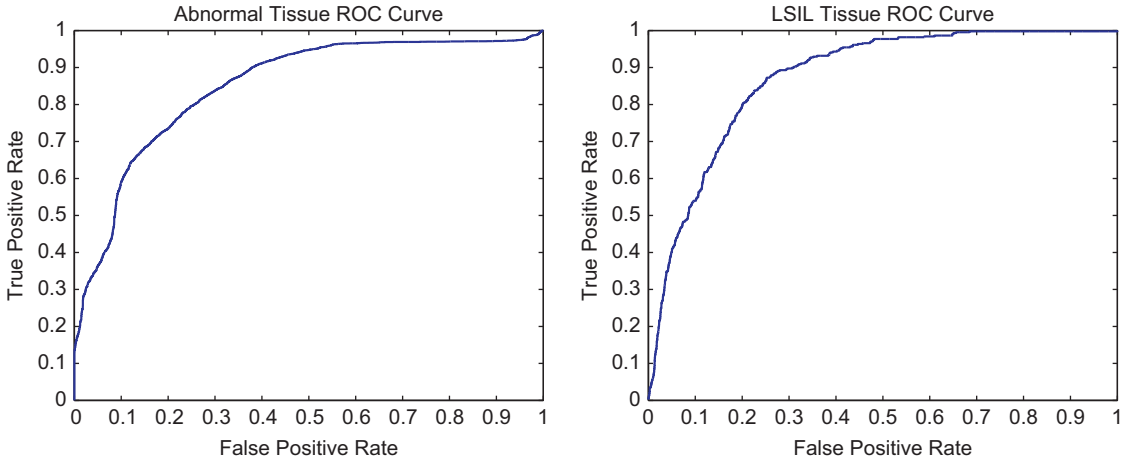

Fig. 8. ROC curves of the SVM classifiers of abnormal (HSIL and LSIL) vs. normal tissue (left) and of LSIL vs HSIL tissue (right).

Even with a robust method to correctly align all images, which is the main contribution of the article, illumination changes are still a major barrier to study the decay effect. The use of an aceto-whiteness measure based on the color saturation has allowed us to retrospectively calculate the acetowhitening decay curve. Future improvements in this area are twofold: on the one hand more tightly controlled illumination settings and/or narrow band wavelength acquisitions as done in [8,7] may be used. On the other hand color calibration of the images together with the use of channels from other color spaces such as LAB or LUV may help.

We have also shown how a useful pixel-wise classifier may be built from the temporal features extracted from the registered image sequences. A standard SVM classifier was used, but other specialized algorithms which combine the temporal features with other image-based measurements such as texture, morphological or vascular features may be used in the future to improve classification and diagnosis.

Conflict of interest statement

None declared.

Acknowledgments

The Image Registration Toolkit was used under Licence from Ixico Ltd. Jan Kybic was supported by Czech Science Foundation Project P202/11/0111. The authors would like to thank Dr. Héctor Gabriel Acosta Mesa for providing the colposcopic sequences of Dataset 2.

Appendix A. Gradient calculation

Using Eq. (1) and the chain rule the gradient of the continuous KL estimated entropy in feature space for each sample is

$$\frac{\partial \mathcal{H}_{KL}^N}{\partial \mathbf{f}(n)} = \frac{D}{2N} \cdot \frac{(\mathbf{f}_{NN}(n) - \mathbf{f}(n))}{\|\mathbf{f}_{NN}(n) - \mathbf{f}(n)\|^2} \tag{A.1}$$

The result of (A.1) is a vector in the feature space originating from the nth sample and pointing toward its nearest neighbor. The intuitive explanation of this is that changing the value of one sample continuously, *i.e.* "sliding" sample n through the feature space, then moving this sample in a straight line toward its nearest neighbor would be the fastest way of minimizing the entropy. In our registration problem all N samples correspond to the feature values extracted from the template and the deformed moving images evaluated at the grid positions. If we represent the moving image by a continuous differentiable function (*e.g.* by splines) then the gradient becomes a function of the grid position. Eq. (A.1) becomes

$$\frac{\partial \mathcal{H}_{KL}^N}{\partial \mathbf{f}(\mathbf{x})} = \frac{D}{2N} \sum_{d=1}^{D} \left(\frac{f_{NN}^d(\mathbf{x}) - f^d(\mathbf{x})}{\|\mathbf{f}_{NN}(\mathbf{x}) - \mathbf{f}(\mathbf{x})\|^2} \right) \nabla_d \mathbf{f}(\mathbf{x}) \tag{A.2}$$

The term $\nabla_d \mathbf{f}$ corresponds to the spatial gradient for each of the features d and depends only on the image and the interpolation method. The complexity of calculating the summation is negligible as the nearest neighbor has already been found to calculate the criterion. Eq. (A.2) is the spatial gradient of $\mathcal{H}_{KL}^N$ at any point when assuming constant topology. The extension to the robust estimator $\mathcal{H}_{DKL}^N$ is trivial:

$$\frac{\partial \mathcal{H}_{DKL}^N}{\partial \mathbf{f}(\mathbf{x})} = \begin{cases} \dfrac{\partial \mathcal{H}_{KL}^N}{\partial \mathbf{f}(\mathbf{x})} & \text{if } \varepsilon < \|\mathbf{f}_{NN}(\mathbf{x}) - \mathbf{f}(\mathbf{x})\| \\ \mathbf{0} & \text{else} \end{cases} \tag{A.3}$$

From this expression it is possible to calculate the gradient of H_{DKL} at any coordinates for elastic or rigid transformations. Fig. A.1 shows the gradient of the joint entropy of two misaligned images calculated analytically and directly through finite differences. Although the results are not exact due to small changes in the tree's topology and noise, the two approximations show the same overall tendencies and an almost exact zero crossing near the correct alignment.

References

[1] C. Mathers, G. Stevens, M. Mascarenhas, W.H. Organization, Global Health Risks: Mortality and Burden of Disease Attributable to Selected Major Risks, World Health Organization, Geneva, Switzerland, 2009.
[2] J. Coste, B. Cochand-Priollet, P. de Cremoux, C. Le Galès, I. Cartier, V. Molinié, S. Labbé, M. Vacher-Lavenu, P. Vielh, Cross sectional study of conventional cervical smear, monolayer cytology, and human papillomavirus DNA testing for cervical cancer screening, BMJ 326 (2003) 733.
[3] T.C.J. Wright, T.J. Cox, L.S. Massad, L.B. Twiggs, E.J. Wilkinson, for the 2001 ASCCP-Sponsored Consensus Conference, 2001 Consensus Guidelines for the Management of Women With Cervical Cytological Abnormalities, JAMA 287 (2002) 2120–2129.
[4] D. Ferris, Modern Colposcopy: Textbook and Atlas, 2nd edition, Kendall Hunt Publishing Company, Dubuque, Iowa, 2002.
[5] H. Lange, D.G. Ferris, Computer-aided-diagnosis (CAD) for colposcopy, Medical Imaging 2005: Image Processing 5747 (2005) 71–84.
[6] B.W. Pogue, H.B. Kaufman, A. Zelenchuk, W. Harper, G.C. Burke, E.E. Burke, D.M. Harper, Analysis of acetic acid-induced whitening of high-grade squamous intraepithelial lesions, Journal of Biomedical Optics 6 (2001) 397–403.
[7] C.J. Balas, G.C. Themelis, E.P. Prokopakis, I. Orfanudaki, E. Koumantakis, E.S. Helidonis, In vivo detection and staging of epithelial dysplasias and malignancies based on the quantitative assessment of acetic acid-tissue interaction kinetics, Journal of Photochemistry and Photobiology B 53 (1999) 153–157.
[8] I.M. Orfanoudaki, G.C. Themelis, S.K. Sifakis, D.H. Fragouli, J.G. Panayiotides, E.M. Vazgiouraki, E.E. Koumantakis, A clinical study of optical biopsy of the uterine cervix using a multispectral imaging system, Gynecologic Oncology 96 (2005) 119–131.
[9] R.P. Woods, Validation of registration accuracy, in: Handbook of Medical Imaging, Academic Press Inc., Orlando, FL, USA, 2000, pp. 491–497.
[10] L.G. Brown, A survey of image registration techniques, ACM Computing Surveys 24 (1992) 325–376.
[11] B. Zitová, J. Flusser, Image registration methods: a survey, Image and Vision Computing 21 (2003) 977–1000.
[12] J. Maintz, M. Viergever, A survey of medical image registration, Medical Image Analysis 2 (1998) 1–36.
[13] J.P.W. Pluim, J.B.A. Maintz, M.A. Viergever, Mutual-information-based registration of medical images: a survey, IEEE Transactions on Medical Imaging 22 (2003) 986–1004.
[14] H. Lester, S.R. Arridge, A survey of hierarchical non-linear medical image registration, Pattern Recognition 32 (1999) 129–149.
[15] H. Lange, R. Baker, J. Håkansson, U.P. Gustafsson, Reflectance and fluorescence hyperspectral elastic image registration, in: J.M. Fitzpatrick, M. Sonka (Eds.), Proceedings of SPIE, Medical Imaging 2004: Physiology, Function, and Structure from Medical Images, 2004, pp. 335–345.
[16] J.D. García-Arteaga, J. Kybic, W. Li, Elastic image registration for movement compensation in digital colposcopy, in: J. Jan, J. Kozumplík, I. Provazník (Eds.), Analysis of Biomedical Signals and Images - Proceedings of Biosignal 2006, EURASIP, VUTIUM Press, Brno, Czech Republic, 2006, pp. 236–238.
[17] H.G. Acosta-Mesa, H.V. Ríos-Figueroa, N. Cruz-Ramírez, A. Marín-Hernández, B. Zitová, R. Hernandez-Jimenez, B.E. Cocotle-Ronzon, E, Hernandez-Galicia, Cervical cancer detection using colposcopic images: a temporal approach, in: Sixth Mexican International Conference on Computer Science, pp. 158–164.
[18] P. King, S. Mitra, B. Nutter, An automated, segmentation-based, rigid registration system for cervigram^{tm} images utilizing simple clustering and active contour techniques, in: CBMS, IEEE Computer Society, 2004, pp. 292–297.
[19] H.-G. Acosta-Mesa, N. Cruz-Ramírez, R. Hernández-Jiménez, Aceto-white temporal pattern classification using k-nn to identify precancerous cervical lesion in colposcopic images, Computers in Biology and Medicine 39 (2009) 778–784.
[20] A. Barreto-Flores, L. Altamirano-Robles, R.M. Morales-Tepalt, J.D. Cisneros-Aragon, Identifying precursory cancer lesions using temporal texture analysis, in: Second Canadian Conference on Computer and Robot Vision, IEEE Computer Society, 2005, pp. 34–39.
[21] J.P.W. Pluim, J.B.A. Maintz, M.A. Viergever, Image registration by maximization of combined mutual information and gradient information, in: MICCAI 2000, Springer-Verlag, London, UK, 2000, pp. 452–461.
[22] R. Gan, A.C.S. Chung, Multi-dimensional mutual information based robust image registration using maximum distance-gradient-magnitude, in: G.E. Christensen, M. Sonka (Eds.), IPMI, Lecture Notes in Computer Science, vol. 3565, Springer, 2005, pp. 210–221.

[23] D. Tomazevic, B. Likar, F. Pernus, Multifeature mutual information, in: J.M. Fitzpatrick, M. Sonka (Eds.), Proceeding SPIE Medical Imaging 2004: Image Processing, Presented at the Society of Photo-Optical Instrumentation Engineers (SPIE) Conference, vol. 5370, 2004, pp. 143–154.
[24] J.D. García-Arteaga, J. Kybic, Regional image similarity criteria based on the Kozachenko-Leonenko entropy estimator, in: CVPRW: Computer Vision and Pattern Recognition Workshops, IEEE, Piscataway, US, 2008, pp. 1–8.
[25] D. Škerl, B. Likar, F. Pernuš, A protocol for evaluation of similarity measures for rigid registration, IEEE Transactions on Medical Imaging 25 (6) (2006) 779–791.
[26] L.F. Kozachenko, N.N. Leonenko, On statistical estimation of entropy of random vector, Problems of Information Transmission 23 (1987) In Russian.
[27] A. Kraskov, H. Stögbauer, P. Grassberger, Estimating mutual information, Physical Review E: Statistical, Nonlinear, and Soft Matter Physics 69 (2004).
[28] J. Kybic, Incremental updating of nearest neighbor-based high-dimensional entropy estimation, in: P. Duhamel, L. Vandendorpe (Eds.), ICASSP, IEEE, 445 Hoes Lane, Piscataway, U.S.A., 2006, p. III-804 DVD proceedings.
[29] J. Kybic, High-dimensional mutual information estimation for image registration, in: ICIP'2004, IEEE Computer Society, 445 Hoes Lane, Piscataway, U.S.A., 2004, p. 4.
[30] G.H. Joblove, D. Greenberg, Color spaces for computer graphics, SIGGRAPH Computer Graphics 12 (1978) 20–25.
[31] R.C. Gonzalez, R.E. Woods, Digital Image Processing, Addison-Wesley Longman Publishing Co., Inc., Boston, MA, USA, 2001.
[32] J. Gu, W. Li, Automatic image quality assessment for uterine cervical imagery, Medical Imaging 2006: Image Perception, Observer Performance, and Technology Assessment 6146 (2006) 61461B.
[33] K. Briechle, U.D. Hanebeck, Template matching using fast normalized cross correlation, in: Proceedings of SPIE: Optical Pattern Recognition XII, vol. 4387, 2001, pp. 95–102.
[34] J.D. García-Arteaga, J. Kybic, Automatic landmark detection for cervical image registration validation, in: M.L. Giger, N. Karssemeijer (Eds.), Proceedings of SPIE, Medical Imaging 2007: Computer-Aided Diagnosis, vol. 6514, SPIE, Bellingham, Washington, USA, 2007, p. 65142S.
[35] J. Kybic, M. Unser, Fast parametric elastic image registration, IEEE Transactions on Image Processing 12 (2003) 1427–1442.
[36] M. Powell, The NEWUOA software for unconstrained optimization without derivatives, in: Large-Scale Nonlinear Optimization, ACM, 2006, pp. 255–297.
[37] M. Powell, UOBYQA: unconstrained optimization by quadratic approximation, Mathematical Programming 92 (2002) 555–582.
[38] M. Galassi, J. Davies, J. Theiler, B. Gough, G. Jungman, M. Booth, F. Rossi, GNU Scientific Library: Reference Manual, Network Theory Ltd., 2003.
[39] K. Godfrey, Compartmental Models and Their Application, Academic Press, London, 1983.
[40] C. Balas, G. Papoutsoglou, A. Potirakis, In vivo molecular imaging of cervical neoplasia using acetic acid as biomarker, IEEE Journal of Selected Topics in Quantum Electronics 14 (2008) 29–42.
[41] H.-G. Acosta-Mesa, N. Cruz-Ramírez, R. Hernández-Jiménez, D.-A. García-López, Modeling aceto-white temporal patterns to segment colposcopic images, in: IbPRIA 2007, Springer-Verlag, Berlin Heidelberg, 2007, pp. 548–555.
[42] D.G. Ferris, R.A. Lawhead, E.D. Dickman, N. Holtzapple, J.A. Miller, S. Grogan, S. Bambot, A. Agrawal, M.L. Faupel, Multimodal hyperspectral imaging for the noninvasive diagnosis of cervical neoplasia, Journal of Lower Genital Tract Disease 5 (2001) 65–72.
[43] D. Rueckert, L.I. Sonoda, C. Hayes, D.L.G. Hill, M.O. Leach, D.J. Hawkes, Nonrigid registration using free-form deformations: application to breast MR images, IEEE Transactions on Medical Imaging 18 (1999) 712–721.
[44] J.A. Schnabel, D. Rueckert, M. Quist, J.M. Blackall, A.D. Castellano-Smith, T. Hartkens, G.P. Penney, W.A. Hall, H. Liu, C.L. Truwit, F.A. Gerritsen, D.L.G. Hill, D.J. Hawkes, A generic framework for non-rigid registration based on non-uniform multi-level free-form deformations, in: MICCAI 2001, Springer-Verlag, London, UK, 2001, pp. 573–581.
[45] C. Studholme, D. Hill, D. Hawkes, An overlap invariant entropy measure of 3D medical image alignment, Pattern Recognition (1998).
[46] G. Yang, C.V. Stewart, M. Sofka, C.-L. Tsai, Registration of challenging image pairs: initialization, estimation, and decision, IEEE Transactions on Pattern Analysis and Machine Intelligence 29 (2007) 1973–1989.
[47] W. Li, R.W. Lieberman, S. Nie, Y. Xie, M. Eldred, J. Oyama, Histopathology reconstruction on digital imagery, in: B. Sahiner, D.J. Manning (Eds.), SPIE Conference Series, vol. 7263, SPIE, 2009, p. 726303.
[48] J.A.K. Suykens, T.V. Gestel, J.D. Brabanter, J.V.B. De Moor, Least Squares Support Vector Machines, World Scientific Pub. Co., Singapore, 2002.
[49] C. Nello, S.-T. John, An Introduction to Support Vector Machines and Other Kernel-Based Learning Methods, Cambridge University Press, Cambridge, 2000.